works against any hypothesis that attributes deep earthquakes in southern Tibet to processes related to subduction.

Large to moderate-sized earthquakes occur at depths of 100 km or more beneath the western Himalayan syntaxis and the western Kunlun Mountains. Such focal depths are likely to be in the mantle, indicating that the uppermost mantle of the continental lithosphere is strong enough to sustain the accumulation of elastic strain required for causing earthquakes. The thickened crust of Tibet appears to vary in thickness by up to 20 km over distances of a few hundred kilometers, so whether every unusually deep earthquake is in the mantle remains uncertain. Nonetheless, a bimodal distribution of focal depths, peaking in the shallow crust and near the Moho, strongly suggests that the two seismogenic regions of the continental lithosphere correspond to maxima in mechanical strength.

References and Notes

1. P. Molnar, P. England, J. Martinod, *Rev. Geophys.* **31**, 357 (1993).
2. L. H. Royden *et al.*, *Science* **276**, 788 (1997).
3. C. Beaumont, R. A. Jamieson, M. H. Nguyen, B. Lee, *Nature* **414**, 738 (2001).
4. P. K. Zeitler *et al.*, *Geol. Soc. Am. Today* **11**, 4 (2001).
5. W.-P. Chen, P. Molnar, *J. Geophys. Res.* **88**, 4183 (1983).
6. P. Molnar, W.-P. Chen, *J. Geophys. Res.* **88**, 1180 (1983).
7. W. F. Brace, D. L. Kohlstedt, *J. Geophys. Res.* **85**, 6248 (1980).
8. S. J. Mackwell, M. E. Zimmerman, D. L. Kohlstedt, *J. Geophys. Res.* **103**, 975 (1998).
9. E. R. Engdahl, R. ven der Hilst, R. Buland, *Bull. Seismol. Soc. Am.* **88**, 722 (1998).
10. C. H. Chapman, J.-Y. Chu, D. G. Lyness, in *Seismological Algorithms: Computational Methods and Computer Programs*, D. J. Doornbos, Ed. (Academic Press, San Diego, CA, 1988), pp. 47–74.
11. C. A. Langston, D. V. Helmberger, *Geophys. J. R. Astron. Soc.* **42**, 117 (1975).
12. J. L. Nábelek, thesis, Massachusettts Institute of Technology, Cambridge, MA (1984).
13. In this notation, an uppercase letter denotes a segment of seismic ray that leaves the earthquake source region as a downgoing *P* or *S* wave. These rays travel to far stations 30° to 90° away ("teleseismic distances") with little complication that arises from major seismic discontinuities bounding the mantle transition zone or from the core-mantle boundary. For each depth phase, the first lowercase letter marks an upgoing ray as it leaves the source at a steep angle. The ray reflects off the free surface and then continues downward toward the station. As such, to a good approximation, the differential timing between *pP* and *P* phases is simply twice the ratio between the focal depth *h* and the average *P*-wave speed between the earthquake and the surface. In cases where either the presence of noise or the limited dynamic range of analog recording hinders detailed modeling of waveforms, we measure differential timing between available depth phases and direct arrivals as supplemental constraints on focal depths (table S2).
14. J. A. Mejia, thesis, St. Louis University, St. Louis, MO (2001).
15. X.-H. Yuan, J. Ni, R. Kind, J. Mechie, E. Sandvol, *J. Geophys. Res.* **102**, 27491 (1997).
16. G. Peglar, S. Das, *Geophys. J. Int.* **134**, 573 (1998).
17. G. Wittlinger *et al.*, *Earth Planet. Sci. Lett.* **221**, 117 (2004).
18. G. Zandt, S. C. Myers, T. C. Wallace, *J. Geophys. Res.* **100**, 10529 (1995).
19. See supporting material on *Science* Online.
20. B. Isacks, P. Molnar, *Nature* **233**, 1121 (1969).
21. W.-P. Chen, H. Kao, in *The Tectonic Evolution of Asia*, A. Yin, M. Harrison, Eds. (Cambridge Univ. Press, Palo Alto, CA, 1996), pp. 37–62.
22. G. Ekström, thesis, Harvard University, Cambridge, MA (1987).
23. L. Zhu, D. V. Helmberger, *Geophys. Res. Lett.* **23**, 435 (1996).
24. J. Jackson, *Geol. Soc. Am. Today* **12**, 4 (2002).
25. N. M. Shapiro, V. Levin, M. H. Ritzwoller, P. Molnar, J. Park, *Eos* **83**, FMS61D (2002).
26. T. J. Owens, G. Zandt, *Nature* **387**, 37 (1997).
27. L. Zhu, thesis, California Institute of Technology, Pasadena, CA (1998).
28. V. Gaur, S. Mitra, K. Priestley, *Eos* **83**, FMS51B (2002).
29. A. Maggi, J. A. Jackson, D. McKenzie, K. Priestley, *Geology* **28**, 495 (2000).
30. W.-P. Chen, J. L. Nábelek, T. J. Fitch, P. Molnar, *J. Geophys. Res.* **86**, 2863 (1981).

31. Supported by the U.S. NSF. This is project Hi-CLIMB contribution I02.

Supporting Online Material

www.sciencemag.org/cgi/content/full/304/5679/1949/DC1
SOM Text
Figs. S1 to S4
Tables S1 and S2
References and Notes

1 March 2004; accepted 13 May 2004

Dynamics of Slow-Moving Landslides from Permanent Scatterer Analysis

George E. Hilley,[1]* Roland Bürgmann,[1] Alessandro Ferretti,[2] Fabrizio Novali,[2] Fabio Rocca[3]

High-resolution interferometric synthetic aperture radar (InSAR) permanent scatterer data allow us to resolve the rates and variations in the rates of slow-moving landslides. Satellite-to-ground distances (range changes) on landslides increase at rates of 5 to 7 millimeters per year, indicating average downslope sliding velocities from 27 to 38 millimeters per year. Time-series analysis shows that displacement occurs mainly during the high-precipitation season; during the 1997–1998 El Niño event, rates of range change increased to as much as 11 millimeters per year. The observed nonlinear relationship of creep and precipitation rates suggests that increased pore fluid pressures within the shallow subsurface may initiate and accelerate these features. Changes in the slope of a hill resulting from increases in the pore pressure and lithostatic stress gradients may then lead to landslides.

Resolving the kinematics of slow-moving, continuously creeping landslides may aid in understanding the mechanics of these hazardous features. The location and extent of some landslides can be determined by geologic mapping, but it has been difficult to develop spatially detailed characterizations of their rates of movement over large areas and time spans (*1*). InSAR (*2*, *3*) can resolve the movement of large (>1 km^2) landslides (*4*); however, coherence problems, inherent error sources, and the spatial and temporal resolution of this method hamper detection and monitoring of landslide features whose rates fluctuate over time. Alternatively, the permanent scatterers InSAR method (PS-InSAR) (*5*–*8*) identifies these scatterers (radar-bright and phase-stable targets such as buildings, utility poles, and rock outcrops) within many (>15) SAR scenes to determine a time series of displacements with high spatial and temporal resolution.

We used 46 scenes acquired by European Remote Sensing Satellites ERS-1 and ERS-2 between 1992 and 2001 to construct a range-change time series for the Berkeley vicinity in the eastern San Francisco Bay area (*9*). Here, the active Hayward Fault (HF) bounds the western margin of the East Bay Hills (EBH), which rise to ~370 m above sea level. The PS-InSAR analysis identified 18,428 PS, which we used in our analysis. Observed range-change rates reflect shallow aseismic right-slip movement along the HF (*8*, *10*, *11*); however, several groups of PS located along the mid-slopes of the EBH display large positive range-change rates (Fig. 1A). To determine the spatial extent and rates of movement of these features, we corrected the range-change rates for the field-measured surface HF slip rates (*12*) and an additional regional, cross-fault offset that may reflect the ~0.4-mm/year uplift of the EBH to the northeast (*13*). The interpolated, adjusted range-change rates resolve at least three patches of large range-rate increases whose locations match those of mapped landslides (*14*) (Fig. 1B). The upslope portions of the slides are commonly located in the vicinity of the HF, whereas downslope portions terminate toward the southwest margin of the EBH. Range-change rates of the southern two landslides were ~5 to 7 mm/year. These rates were measured in the direction of the look-angle of the satellite, so there was insufficient information to resolve all of the components of the displace-

[1]Department of Earth and Planetary Science and Berkeley Seismological Laboratory, University of California, Berkeley, CA 94720, USA. [2]Tele-Rilevamento Europa, Via Vittoria Colonna 7, 20149 Milano, Italy. [3]Dipartimento di Elettronica e Informazione, Politecnico di Milano, 20133 Milano, Italy.

*To whom correspondence should be addressed. E-mail: hilley@seismo.berkeley.edu

ment or velocity vectors. However, assuming that most of the displacement along these landslides follows the average 4° downhill slope, the measured range-change rates imply sliding at velocities of 27 to 38 mm/year (*15*).

The time series of range-change rates allowed us to explore the relationship between precipitation and slide movements. Cumulative precipitation and 20-day averaged precipitation rates were calculated using data from the Richmond meteorological station (*16*), about 5 miles north of the landslides (*8*). Between 1992 and 2001, annual precipitation averaged 0.61 m/year, with 95% of the precipitation falling between the months of October and April. At values of seasonal cumulative precipitation less than 0.5 m, higher precipitation intensities led to proportionally increased slide displacements, whereas larger amounts of yearly precipitation resulted in less movement than expected on the basis of dryer years (*8*, *17*).

The 1997–1998 El Niño event saw a ~200% increase in seasonal precipitation; peak 20-day-averaged precipitation intensity exceeded 6 m/year, about 10 times the long-term annual average. Seventeen scenes acquired during the El Niño event and the following year resolve the details of the movements of the landslides in response to the wet year (Fig. 2). In the season preceding the enhanced El Niño precipitation, range-change rates in the vicinity of the northern and middle slides were low and often difficult to distinguish from the surrounding areas, while the southern slide moved between January and July 1997. With the onset of the El Niño rains, we could not detect movement of the mapped landslides even ~3 months into the rainy season. Between November 1997 and April 1998, range-change rates along the middle slide accelerated to maximum values of 35 mm/year. In the following dry season (May to November 1998), movement along the slides was not detectable. During the El Niño, the peak yearly-averaged range-change rates were ~10 mm/year, about 30% higher than typical years. However, the 1997–1998 El Niño seasonal displacements were not as high as would have been predicted from extrapolation of trends observed at lower cumulative precipitation (*8*). Total precipitation during the following year (1999) was only 35% of that during El Niño, which is generally reflected in the 10 to 20 mm/year decrease in the peak range-change velocities of the middle and southern slides during the wet season. The north slide moved ~20 mm/year (greater than during the wetter El Niño time by ~5 to 10 mm/year) during 1999 (*8*, *18*).

The association of landslide motion with high precipitation indicates that near-surface groundwater flow may play a role in the initiation and acceleration of sliding. In particular, increased flow in the near-surface groundwater system and eventual saturation may increase pore pressures, decrease the effective strength of the failure surface, and trigger movement (*19*, *20*). However, the ~3-month time lag observed between the onset of precipitation and acceleration of the slides during the El Niño season suggests that the near-surface groundwater system acts to buffer the effects of intense and sustained precipitation early in the wet season. Specifically, the time associated with saturating the groundwater system appears to discourage failure along the slides early in the wet season and during relatively dry years. The nonlinear response of landslide movement to seasonal precipitation (*8*) suggests that saturation of the near-surface hydrologic system may occur during wet years, which may act in concert with increased sliding resistance at higher velocities to reduce the sensitivity of creep rates to total seasonal precipitation.

Whereas the seasonal acceleration of sliding is closely tied to rainfall, the location of the slides on the slopes of the EBH is determined by slope increases caused by long-term tectonic uplift along the HF. The head scarps of the landslides generally are located upslope of a ~150% increase in average hill-slope angles in the vicinity of the HF. This observation suggests that there is likely a causal relationship between the increases in slope (perhaps driven by uplift northeast of the HF) and the location of these landslides.

To test the hypothesis that the landslides are tied to slope increases near the HF, we focus on the topography of the middle landslide where

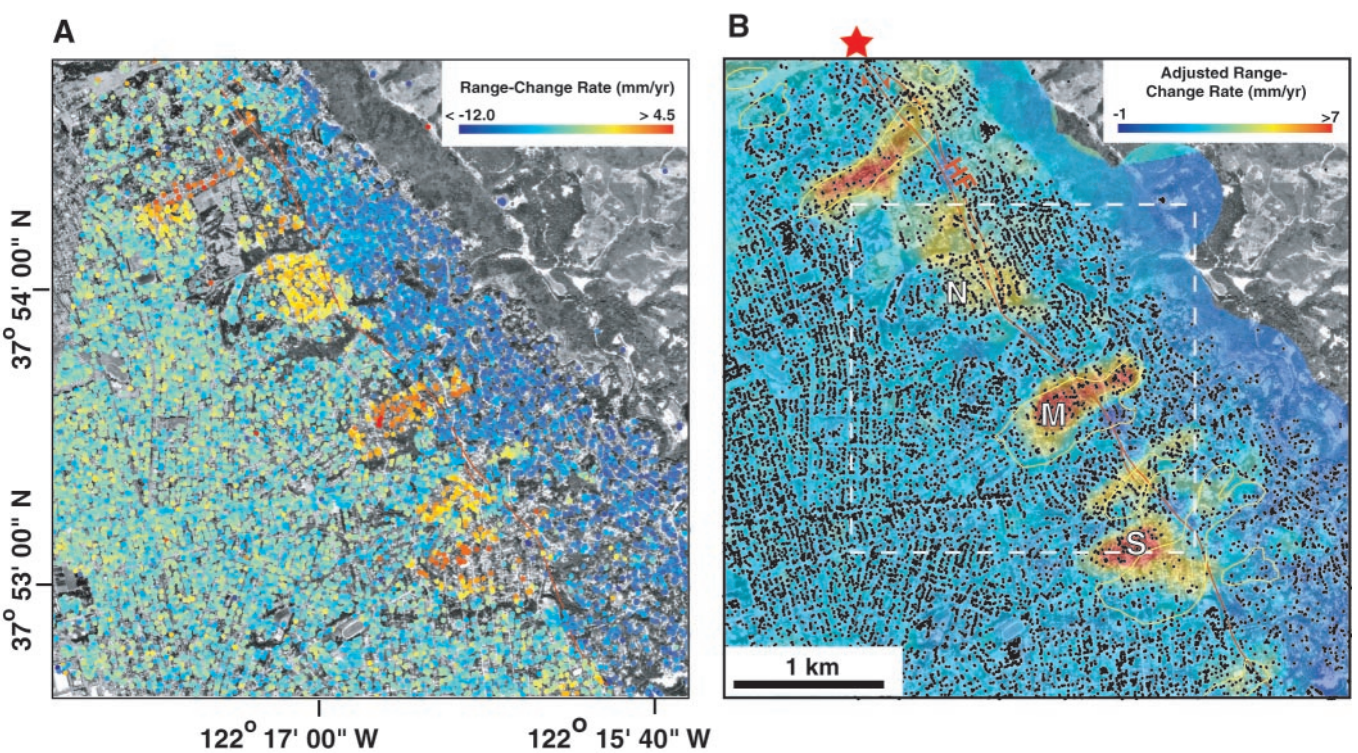

Fig. 1. (**A**) Map view of PS-InSAR range-change rate measurements for the study area. Underlying image is an orthorectified air photo of the area; HF trace is indicated by a red line (*28*). (**B**) Map view of interpolated range-change rates (colors) adjusted for shallow creep (4 to 5 mm/year) along the HF and uplift (0.4 mm/year) of the EBH (black dots show PS locations). Yellow outlines show the location of mapped active landslides (*14*). Dashed box indicates the extent of panels in Fig. 2. N, M, and S denote locations of the northern, middle, and southern landslides investigated. Red star shows location of M_L = 4.1 earthquake on 4 December 1998 (*8*, *18*).

this relationship is most pronounced. Landslides can be triggered by the weight of the overlying material and fluid pressure changes driven by groundwater flow. In soil or rock near the surface, where cohesion is negligible, failure ensues when the shear traction (τ) acting along a potential failure surface exceeds the normal traction (σ) scaled by the material friction coefficient (μ) (*21*). The presence of groundwater increases the pore fluid pressure (p) along this potential failure surface and reduces the normal traction that would otherwise discourage failure (*19*). To quantify these competing effects, we use the Coulomb failure function (*CFF*) (*21*) that gauges the propensity for failure in the near-surface layer:

$$CFF = |\tau| - \mu(\sigma + p) \qquad (1)$$

Here, compressive tractions (defined as negative) are generally opposed by positive pore pressures. When $CFF \geq 0$, the near-surface material will fail as a landslide.

We simulated the approximate surface geometry of the middle slide with a model (*8*) that couples lithostatic stresses (*22*, *23*) with pore pressures generated by steady groundwater flow (*24*–*26*). From these models, we calculated the stress tensor for every point near the surface. The shear and normal tractions in Eq. 1 vary with the orientation of the potential failure plane, and so we let this orientation vary at each point so as to maximize the value of *CFF* (CFF_{max}) (*21*) (Fig. 3). Values of CFF_{max} close to zero should outline the approximate extent and geometry of new landslide failure surfaces. The combined stresses due to gravity and pore pressures move the near-surface region along the entire hill slope close to or beyond their failure limit. However, the change in slope in the vicinity of the HF causes a deepening of the failure zone downslope of the head scarp of the slides. Finally, the failure envelope shallows both toward the top and bottom of the topography. Therefore, the model results indicate that failure is promoted within the mid-slopes of the topography and may be exacerbated by slope changes in these areas. These predictions agree with the observed location of the landslides (*27*), indicating that the lithostatic stresses and groundwater flow are important components of the failure and movement of these slides.

Our study demonstrates a method that can resolve detailed seasonal variations in the movement of slow-moving landslides. Our analysis of these features shows that their location may be influenced by modification of near-surface groundwater flow by tectonically induced slope changes. This flow is, in turn, modulated by seasonal increases in precipitation. The progressive saturation of this near-surface groundwater system during the wet season may induce a lag between the beginning of intense rains and acceleration of the landslides. The relationship between seasonal precipitation and slide movement is nonlinear, in that rainfall above certain amounts may not cause additional pore-pressure increases and slip acceleration of these types of landslides.

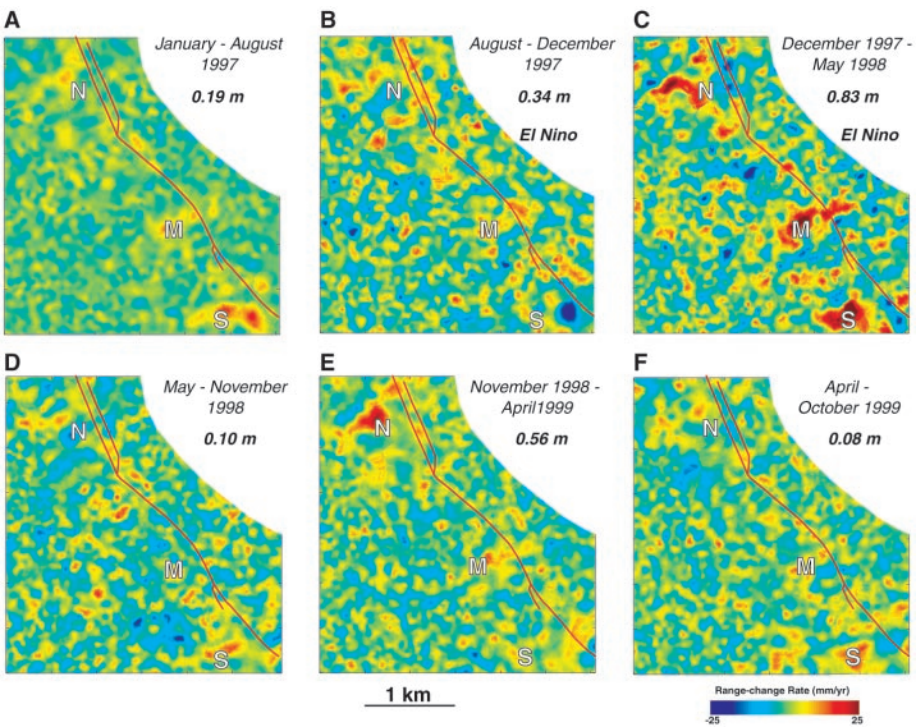

Fig. 2. Time-dependent range-change rates from 1997 to 2000 (panels span time indicated in upper right corner), including the 1997–1998 El Niño period. See Fig. 1 for location of panel. Bold italic numbers denote the amount of cumulative precipitation experienced by the area during the elapsed time shown. The HF is shown as a thin red line in each panel.

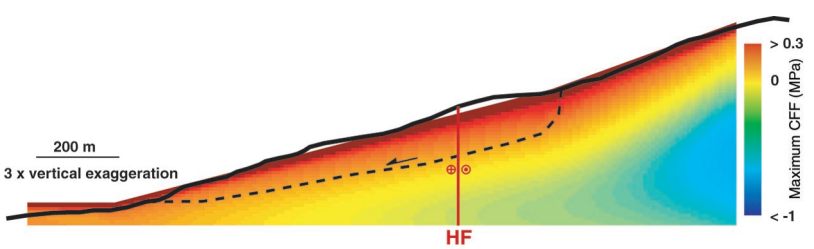

Fig. 3. Topographic profile of the middle slide (heavy black line), inferred location of slide base (heavy dashed line), and modeled value of CFF_{max} (color scale bar on right) (*8*, *21*). Here, slopes along the lower and upper portions of the hills increase from 4.2° to 6.3°. Orientation of optimal failure plane in the near-surface region varies slightly with downslope position but is close to ~15° downslope. Positive values of *CFF* indicate regions expected to undergo brittle failure; negative values of this parameter indicate mechanically stable regions.

References and Notes

1. K. Vonder Linden, *Eng. Geol.* **27**, 301 (1989).
2. D. Massonnet, K. L. Feigl, *Rev. Geophys.* **36**, 441 (1998).
3. R. Bürgmann, P. A. Rosen, E. J. Fielding, *Annu. Rev. Earth Planet. Sci.* **28**, 169 (2000).
4. B. Fruneau, J. Achache, C. Delacourt, *Tectonophysics* **265**, 181 (1996).
5. A. Ferretti, C. Prati, F. Rocca, *IEEE Trans. Geosci. Remote Sens.* **28**, 2202 (2000).
6. A. Ferretti, C. Prati, F. Rocca, *IEEE Trans. Geosci. Remote Sens.* **39**, 8 (2001).
7. C. Colesanti, A. Ferretti, F. Novali, C. Pratti, F. Rocca, *IEEE Trans. Geosci. Remote Sens.* **41**, 1685 (2003).
8. See supporting data at *Science* Online.
9. The area analyzed by this study extends from 122°18′15.6″ to 122°12′49.212″W and from 37°52′27.9″ to 37°55′32.4″N.
10. R. Bürgmann *et al.*, *Science* **289**, 1178 (2000).
11. D. A. Schmidt, thesis, University of California, Berkeley (2002).
12. J. J. Lienkaemper, J. S. Galehouse, R. W. Simpson, *Geophys. Res. Lett.* **28**, 2265 (2001).
13. After correction for shallow creep along the northern HF (4.3 to 4.5 mm/year) (*28*), a cross-fault range-change residual of ~0.4 mm/year was removed using the means of nonlandslide points on each side of the fault. Finally, we detrended the range-change rates in the direction perpendicular to the strike of the fault to remove a fault-perpendicular ramp in the data.
14. A. Kropp and Associates, *Landslides of the Berkeley Hills* [map] (1995). Map available at http://www.akropp.com/pdf%20files/bh%20slide%20map.pdf
15. Sliding velocities were computed by projecting the unit vector of the downslope sliding direction (average slope angle 4°; downslope direction vector v = [−0.66 −0.75 −0.07], where vector is defined as [x y z], positive-up, right-handed coordinate system) onto the unit vector defining the look direction of the satellite (azimuth = 13.8°; off-vertical axis = 23.0°; satellite look direction vector u = [−0.23 0.06 −0.97]) using the equation $S = 1/(v^T u)$, where S is the amplification of the range-change rate when projected into the downslope direction, and v^T is the trans-

pose of v. This computation yields a downslope projected velocity of 5.5 times the measured range-change rate.
16. Data obtained from the NOAA National Climatic Data Center (http://cdo.ncdc.noaa.gov/CDO/cdo).
17. Time intervals between each pair of SAR satellite scenes varied from year to year. To avoid bias in seasonal cumulative displacements, we manually inspected the range-change time series and found that displacement of the slides occurred almost exclusively during the wet season, so displacements from the wet season capture the total yearly change.
18. The north slide was closest to a M_L (catalog local magnitude) = 4.1 earthquake on 4 December 1998. Although the temporal resolution of the time series is insufficient to clearly resolve triggered sliding caused by this event, the seasonal displacement along the north slide during this period was anomalously high given the amount of precipitation during this interval (*8*), possibly indicating that the sliding may have been accelerated by seismic shaking.
19. K. Terzaghi, in *Proceedings of the International Conference on Soil Mechanics and Foundation Engineering* (Graduate School of Engineering, Harvard University, Cambridge, MA, 1936), vol. 1, pp. 54–55.
20. R. A. Freeze, J. A. Cherry, *Groundwater* (Prentice-Hall, Englewood Cliffs, NJ, 1979).
21. J. C. Jaeger, N. G. W. Cook, *Fundamentals of Rock Mechanics* (Chapman and Hall, New York, 1979).
22. S. J. Martel, J. R. Muller, *Pure Appl. Geophys.* **157**, 989 (2000).
23. D. F. McTigue, C. C. Mei, *J. Geophys. Res.* **86**, 9268 (1981).
24. M. G. McDonald, A. W. Harbaugh, *A Modular, Three-Dimensional Finite-Difference Ground-Water Flow Model: U.S. Geological Survey Techniques of Water Resource Investigations, bk. 6* (U.S. Geological Survey, Washington, DC, 1988).
25. R. M. Iverson, M. E. Reid, *Water Resour. Res.* **28**, 925 (1992).
26. M. E. Reid, R. M. Iverson, *Water Resour. Res.* **28**, 939 (1992).
27. Head scarps of these types of slides show evidence of fissuring and failure in tension, so *CFF* may not provide direct information about where this fissure may reach the surface. However, opening localizes where displacement gradients along the landslide failure surface are large, and so we expect these features to root into the deeper landslide surface where *CFF* is large.
28. J. J. Lienkaemper, *USGS Misc. Field Studies Map MF-2190* (1993).
29. ERS data are courtesy of the European Space Agency (in the framework of ESA-ESRIN Contract 13557/99/I-DC) as well as the WInSAR consortium. This is Berkeley Seismological Laboratory contribution number 04-06.

Supporting Online Material
www.sciencemag.org/cgi/content/full/304/5679/1952/DC1
Materials and Methods
Fig. S1
References

6 April 2004; accepted 18 May 2004

Abrupt Tropical Vegetation Response to Rapid Climate Changes

Konrad A. Hughen,[1]* Timothy I. Eglinton,[1] Li Xu,[2] Matthew Makou[2]

Identifying leads and lags between high- and low-latitude abrupt climate shifts is needed to understand where and how such events were triggered. Vascular plant biomarkers preserved in Cariaco basin sediments reveal rapid vegetation changes in northern South America during the last deglaciation, 15,000 to 10,000 years ago. Comparing the biomarker records to climate proxies from the same sediment core provides a precise measure of the relative timing of changes in different regions. Abrupt deglacial climate shifts in tropical and high-latitude North Atlantic regions were synchronous, whereas changes in tropical vegetation consistently lagged climate shifts by several decades.

In order to evaluate the relative roles of high and low latitudes in initiating and propagating abrupt global climate changes, we need precise information regarding the relative timing of abrupt changes in different regions. Dating uncertainties, however, are typically too large to constrain the timing of the briefest decadal events in records from different sites (*1*–*4*). Another approach is to identify high- and low-latitude climate proxies in the same high-resolution record, and determine the relative timing of changes stratigraphically (*3*–*6*). For instance, increased methane concentrations attributed to the expansion of tropical wetlands (*7*) have been measured in air trapped in Greenland ice and used to infer shifts to warmer and/or wetter tropical climate during the abrupt Glacial/Bølling and Younger Dryas/Preboreal transitions (*3*, *4*). Temperature changes over Greenland were also reconstructed from the same samples using nitrogen and argon isotopes, allowing the precise identification of relative timing for rapid changes between the tropics and high latitudes. The tropics were found to lag Greenland by 20 to 30 and 0 to 30 years for the Bølling and Preboreal warmings, respectively (*3*, *4*), favoring a North Atlantic trigger at least for the Bølling event (*4*). In similar studies, radiocarbon measured in planktonic foraminifera from tropical Cariaco basin sediments was shown to have increased steeply during the onset of Younger Dryas cooling (*5*, *6*). Atmospheric concentration of cosmogenic beryllium-10 does not show a similar increase during the Younger Dryas onset (*8*), suggesting that the ^{14}C increase was not caused by changes in production rate, but that it instead reflects an abrupt decrease in high-latitude North Atlantic Deep Water (NADW) formation and export (*5*, *6*, *9*). In addition, relative reflectance (gray scale) and laminae thickness from the same sediments reveal rapid shifts in Cariaco upwelling and trade-wind intensity caused by shifts in the mean position of the Intertropical Convergence Zone (*2*, *5*, *6*). Direct comparison of Cariaco radiocarbon and gray-scale data showed that high- and low-latitude climate shifts during the onset of Younger Dryas cooling were synchronous within 10 years (*6*), and thus allows either a North Altantic or a tropical trigger for this rapid climate cooling. If abrupt deglacial warming and cooling events were manifestations of the same millennial-scale shifts in global climate, this subtle discrepancy in timing between Cariaco and Greenland data must be resolved before we can understand the mechanisms responsible for abrupt climate change.

The delayed increase in atmospheric methane following abrupt warmings may have been caused by the release of gas hydrates rather than expansion of tropical wetland vegetation (*10*). However, studies have shown fluctuations in deglacial tropical moisture balance similar in timing to the Bølling/Allerød and Younger Dryas oscillations in the North Atlantic region (*11*–*17*), supporting tropical wetlands as the source for the atmospheric methane signal. Specifically, detailed pollen records from Central and northern South America (*11*, *12*), including the Cariaco basin watershed (*13*, *14*), show that vegetation shifted between predominantly dry grasslands during the Glacial and Younger Dryas periods, and wet montane forest during the Bølling/Allerød and Preboreal periods. The lag of the methane increase behind Greenland warming may have occurred because the time scale necessary for tropical wetland expansion and development of anoxia following a climate shift may be longer than previously thought (*4*, *18*). However, the response time for changes in vegetation fol-

[1]Department of Marine Chemistry and Geochemistry, [2]Department of Geology and Geophysics, Woods Hole Oceanographic Institution, Woods Hole, MA 02543, USA.

*To whom correspondence should be addressed. E-mail: khughen@whoi.edu

Supporting Online Material:

InSAR Permanent Scatterer methods:

The PS-InSAR method (*S1,S2)* improves our ability to determine mm-scale displacements of individual features on the ground using all data collected over the target area by a SAR satellite (such as the European Space Agency's Earth Remote Sensing, ERS-1&2 spacecraft upon which we rely in this study). InSAR methods estimate changes in the distance from the satellite to the ground in the look-direction of the satellite by measuring phase changes in the radar signal between different satellite passes. The steep look-angle (23° off vertical) of the satellite makes this scalar measurement particularly sensitive to the vertical component of displacements.

Several sources of random and systematic errors may decrease the resolution of deformation measurements. Changes in dielectric properties of the surface between satellite passes, errors in digital topography, and phase changes associated with changes in atmospheric properties between satellite passes may act to distort the deformation field inferred from the SAR interferogram (*S3, S4*). Rather than reduce the spatial resolution or stack interferograms to improve signal-to-noise (as is commonly done in traditional InSAR methods), PS-InSAR methods identify radar-bright and radar-phase stable points (i.e., permanent scatterers) that exist within a radar scene and more than about 15 SAR acquisitions to separate a modeled deformation rate, atmospheric, and elevation error components of the range-change measurement (*S5*). Radar bright targets are those in which a variety of orientations of incident radiation may be reflected back, and so these points provide the most consistently reliable radar returns in the image. In addition, changes in phase of these permanent scatterers are required to be far less than $2\pi\lambda$ (λ is radiation wavelength) to prevent ambiguities in the inferred range change. Components of errors are isolated by noting the DEM errors may not be correlated in space, but are highly correlated in time, while atmospheric effects may be correlated in space but not over time. Deformation may be modeled as a linear This process generally increases the spatial and temporal sampling resolution of displacement measurements as well as the measurement precision. The PS-InSAR method can measure surface motions at a level of < 1 mm/yr and can resolve very small-scale features, including motions of individual scatterer targets, not previously recognized in traditional SAR interferometry over the San Francisco Bay area (*S6).*

Precipitation and movement of slides

We show the cumulative precipitation observed at the Richmond meteorological station for the entire period spanned by SAR measurements (Sfig 1A) and the El Niño season (Sfig1B). Using these data, we calculated the 20-day averaged precipitation intensity during the El Niño season. For reference, the time-intervals shown in Fig. 2 of the text are labeled as A—F in Sfig 1B. We found that during the 1980—2004 time interval, approximately 95% of all precipitation fell during the months of October—April.

To discern the relationship between total seasonal precipitation and total slide movement, we identified intervals for which seasonal displacements could be measured based on the InSAR time series. We label each interval with an asterisk in Sfig1A, with the interval bounds denoted by vertical lines. For each slide (north, middle, south), we selected ten points along the slide and computed their average displacement during each interval. Using this information, we observed a non-linear relationship between seasonal cumulative precipitation and seasonal slide motion (Sfig. 2). Specifically, during years experiencing < 0.5 m of cumulative precipitation, increased precipitation leads to commensurate increases in seasonal displacement. However, during the 1997—1998 El Niño event, increased precipitation led to only slightly increased displacements along each of the slides. This decreasing sensitivity of slide movement to larger values of seasonal cumulative precipitation likely reflects the progressive saturation of the near-surface groundwater system. During dry years, a large proportion of the total precipitation likely infiltrates, acting to increase pore-pressures in the subsurface. However, during high-precipitation El Niño years, the near-surface becomes saturated, and so all excess precipitation generates surface runoff, rather than infiltrates to produce higher pore-pressures in the subsurface.

Interestingly, a M_L=4.2 earthquake occurred on December 12, 1998 in close proximity to the north slide. The temporal resolution of our time-series is insufficient to resolve instantaneous movement or subsequent acceleration of this landslide. However, the time series does reveal that an anomalously high seasonal displacement occurred during the October 1998—April 1999 interval (Sfig. 2). This high displacement is not easily explained by natural variation in seasonal displacements observed during other years and along the other two slides. Therefore, it is possible that the InSAR-PS time series records acceleration of sliding due to seismic shaking during this event.

Model construction and setup:

In this study, we model lithostatic stresses and pore-pressures along hill-slopes with similar geometry to those of the EBH, we combined two different models that calculated each of these sources of stress. While this model is simple and does not take into account seasonal variations in groundwater flow patterns, it serves as a useful approximation of the conditions that may localize deformation along the mid-slopes of the EBH. First, we modified a version of TWODD (*S7*), a two-dimensional boundary element model that computes stresses and displacements within a homogeneous elastic full-space and implemented the modifications of Martel and Muller (*S8*; discussed below). Pore-pressures were calculated using the Modflow finite-difference groundwater flow model (*S9*). Details of the methods, geometry and boundary conditions of each model are discussed below.

Lithostatic stress model:

Methods:

Following the modifications of Martel and Muller (*S8*), we considered lithostatic stresses by explicitly modeling the free (i.e., traction-free) surface as a series of dislocations. These dislocations were each 10 meters long (in model space) and shared common vertices. To avoid edge effects near the termination of the free-surface dislocations, we extended these dislocations to -4/+2.5 times the horizontal dimension of the considered model space. This is equivalent to -20/+12.5 times the vertical dimension of the model space, and so our results are virtually free of edge effects that may be seen within several model-length-scales of the edges of the dislocations. Boundary conditions along each dislocation were determined by resolving the far-field boundary conditions (discussed below) onto each element, reversing these tractions, solving for the displacements resulting from these tractions, and finally superposing lithostatic loading conditions. This operation yields a traction-free surface that satisfies the remote boundary conditions discussed below. Using the computed displacement discontinuities, we calculated the stress tensor every 10 and 2.5 meters in the horizontal and vertical directions underneath the sloping portion of the surface. To ensure that our methods were implemented correctly, we duplicated the model geometries and boundary conditions of Martel and Muller (*S8*), Savage and Swolfs (*S10*), and Iverson and Reid (*S11*), and found similar results.

Geometry:

As mentioned previously, we modeled the free surface as 700 connected displacement discontinuities subject to traction boundary conditions. Each dislocation was 10 meters long. Dislocations from –4000 to –200 m (in model space) were horizontal, approximating an infinitely long left free-surface boundary located at y = 0. From –200 to – 900 m, the connected dislocations sloped 4.23 degrees, simulating the lower portion of the hill-slope. From 900 to – 1400 m, the dislocations' slopes steepened to 6.28 degrees to simulate the steeper slopes above the HF. From 1400 to 9000 m, horizontal dislocations were specified at the height of the final element (135 m). Finally, to satisfy the requirements of the remote boundary conditions, from 9,000 to 10,000 m, we used a traction-free, sloping element that extended from the elevation of the elements at 135 m to zero. While the area to the northeast of the western ridge of the EBH is incised, the mean topography does not begin to decrease until ~5 km to the northeast. Therefore, it is more appropriate to model the topography as a constant height area than a symmetric ridge (e.g., *S10*—*S13*).

Boundary Conditions:

Following Martel and Muller (*S8*), we prescribed remote boundary conditions that required the crust to remain laterally constrained in the horizontal dimension. The remote boundary conditions that satisfy this requirement are (*S14*):

$$\sigma_{xx(remote)} = [\upsilon / (1-\upsilon)]\ \rho g y + \sigma_{xx(remote\text{-}tectonic)}$$
$$\sigma_{yy(remote)} = \rho g y + \sigma_{yy(remote\text{-}tectonic)}$$
$$\sigma_{xy(remote)} = \sigma_{xy(remote\text{-}tectonic)}$$

where υ is Poisson's ratio, g is the acceleration due to gravity [L/t^2], y is the vertical length (positive upward), and $\sigma_{xx(remote\text{-}tectonic)}$, $\sigma_{yy\ (remote\text{-}tectonic)}$, and $\sigma_{xy(remote\text{-}tectonic)}$ are the far-field remote tectonic stresses. In this problem, we focus on the effects of lithostatic loading and so let $\sigma_{xx(remote\text{-}tectonic)}$, $\sigma_{yy\ (remote\text{-}tectonic)}$, and $\sigma_{xy(remote\text{-}tectonic)} = 0$. This remote stress tensor was resolved onto the center of each free-surface element and the traction value inverted to yield the complimentary stress before superposition of the lithostatic stresses encapsulated in the remote boundary conditions.

Groundwater flow model:

Methods

We used the Modflow (*S9*) finite-difference groundwater flow model to calculate subsurface pore-pressures along the hill-slope. Because few data are available on the groundwater table level in the vicinity of the landslides, following (*S15*), we calculated the maximum pore-pressure value along the slopes by assuming that the entire slope and subsurface layer is saturated. While our analysis shows that saturation of this layer probably takes several months to accomplish, this calculation is appropriate for the last three months of the wet season when ground saturation is probably achieved. In earlier parts of the rainy season, or during dry years in which the ground surface does not saturate, we expect the extent of the saturated landscape (where the groundwater table reaches the surface) to be concentrated in the topographically lower portions of the landslides (*S15*). Full characterization of how seasonal precipitation effects the saturation of this layer is beyond the scope of this study, but may be analyzed using coupled saturated-unsaturated flow models in which hydrologic properties of the EBH are constrained by extensive field measurements not currently available. We computed the steady-state total head distribution along the slopes and subtracted the elevation head from this value to obtain the fluid (i.e., pore) pressure. These values were then used with the CFF described in the text to compute propensity for failure along the hill slopes.

Geometry and Boundary Conditions

The model domain was 7.4 km x 640 m, gridded at 10 m and 2.5 m increments, in the horizontal and vertical dimensions, respectively. Finite-difference cells above the free surface were identified and labeled as inactive during the computations. The surface boundary condition for the saturated medium was prescribed as a constant elevation that reflected the topographic elevation of the surface (*S11*). Therefore, at the surface, the total head was only composed of the elevation head, with no pore pressure. In contrast to the symmetric models of Iverson and Reid (*S11*), the presence of the San Francisco Bay to the southwest of the EBH provides a means of moderating water-table levels, and so the left-hand boundary was set as a constant-elevation boundary condition whose value was equal to the elevation of each point along the boundary. Finally, following Iverson and Reid (*S11*), we set the bottom and right-hand boundary conditions equal to no-flow boundary conditions. These boundary conditions produced similar results to Iverson and Reid (*S11*); however, the constant-elevation boundary condition at the left-hand side of the model restricted the upward flow of water that is expected in the presence of a no-flow boundary (*S11*).

Failure Criteria:

For the initiation of new slides, we considered the maximum CFF, which allows the orientation of the failure plane to vary so as to maximize the CFF value at each point. In this case, slip along the failure surface occurs when the shear traction exceeds the frictionally-scaled normal traction. Hence we predict the most likely location of failure, rather than develop a criterion that predicts sliding magnitude once failure has ensued. However, once failure has occurred within the medium, displacements will accrue when the CFF ≥ 0 for the specific plane of failure that has been created. In Figure 3 of the text, the orientation of the failure plane is sub-parallel to the lower hill-slope. To investigate how the CFF changes as the result of failure along the landslide surface, we resolved the shear and normal tractions onto a surface oriented parallel to the lower section of the hill-slope (4.23°), adjusted the normal traction for pore-pressures, and calculated the CFF for this case. We show the results in Sfig. 3. We note that while there are some differences in the details of the CFF distribution, the general trends identified by the maximum CFF are also present in the near-surface CFF resolved onto the 4.23° failure plane. Since the CFF distributions are similar, we conclude that inferences of likely failure locations are robust within a range of likely failure surface orientations.

Figure Captions:

Sfig. 1. (A) 1992—2001 cumulative precipitation (solid line) from the Richmond, CA weather station. Vertical arrows denote the time at which SAR images were acquired and range-change displacements determined. Asterisks and thin vertical lines denote the period of time used to calculate the cumulative precipitation and displacement shown in Sfig. 2. (B) Cumulative precipitation (solid line), 20-day averaged precipitation rate (dashed line), and time-series intervals (A—F in Fig. 4, bounded by vertical dotted lines) used to compute landslide velocities in Fig. 2. Letters underneath x-axis denote months during the year.

Sfig. 2. Relationship between seasonal cumulative precipitation and displacement for the three slides labeled in Figure 1 (rainy season intervals shown in Sfig. 1A). Gray areas encompass groups of points from the same landslide. Points with 0.82 m of seasonal cumulative precipitation represent 1997—1998 El Niño wet season. During years that have less than 0.5 m of cumulative precipitation, landslide displacements increase. However, during the wet El Niño year in which seasonal cumulative precipitation was large, average slide displacements were lower than would be expected based on dryer years. This non-linearity in slide displacement may result from saturation of the near-surface groundwater system, leading to runoff generation during extremely wet years that does not accelerate motion of the landslides.

Sfig. 3. CFF computed for a failure surface assumed to be sub-parallel to the lower portion of the topographic surface (4.23°). All notation similar to that used in Fig. 3 of text.

Supplementary Information Notes:

S1. A. Ferretti, C. Prati, F. Rocca, *IEEE Trans. Geosci. Remote Sens.*, **28**, 2202 (2000).

S2. A. Ferretti, C. Prati, F. Rocca, *IEEE Trans. Geosci. Remote Sens.*, **39**, 8 (2001).

S3. Massonnet, D. and K. L. Feigl, *Rev. Geophys.*, **36**, 441 (1998).

S4. Bürgmann, R., P. A. Rosen, and E. J. Fielding, *Ann. Rev. Earth Planet. Sci.*, **28**, 169 (2000).

S5. C. Colesanti, A. Ferretti, F. Novali, C. Pratti, F. Rocca, *IEEE Trans. Geosci. Remote Sens.*, **41**, 1685 (2003).

S6. Bürgmann, R., et al., *Science*, **289**, 1178 (2000).

S7. S. L. Crouch and A. M. Starfield, *Boundary Element Methods in Solid Mechanics*, (Allen and Unwin, London), (1983).

S8. S. J. Martel and J. R. Muller, *Pure and App. Geophys.*, **157**, 989 (2000).

S9) M. G. McDonald and A. W. Harbaugh, *A modular, three-dimensional finite-difference ground-water flow model: U.S. Geological Survey Techniques of Water Resource Investigations, bk. 6* (U. S. G. S., Washington, D. C.), (1988).

S10) W. Z. Savage and H. S. Swolfs, *J. Geophys. Res.*, **91**, 3677 (1986).

S11) R. M. Iverson and M. E. Reid, *Water Resour. Res.*, **28**, 925 (1992).

S12) M. E. Reid and R. M. Iverson, *Water Resour. Res.*, **28**, 939 (1992).

S13) D. F. McTigue and C. C. Mei, *J. Geophys. Res.*, **86**, 9268 (1981).

S14) J. C. Jaeger and N. G. W. Cook, *Fundamentals of Rock Mechanics* (Chapman and Hall, NY), (1979).

S15) R. A. Freeze and J. A. Cherry, *Groundwater* (Prentice Hall, Englewood Cliffs, NJ), (1979).

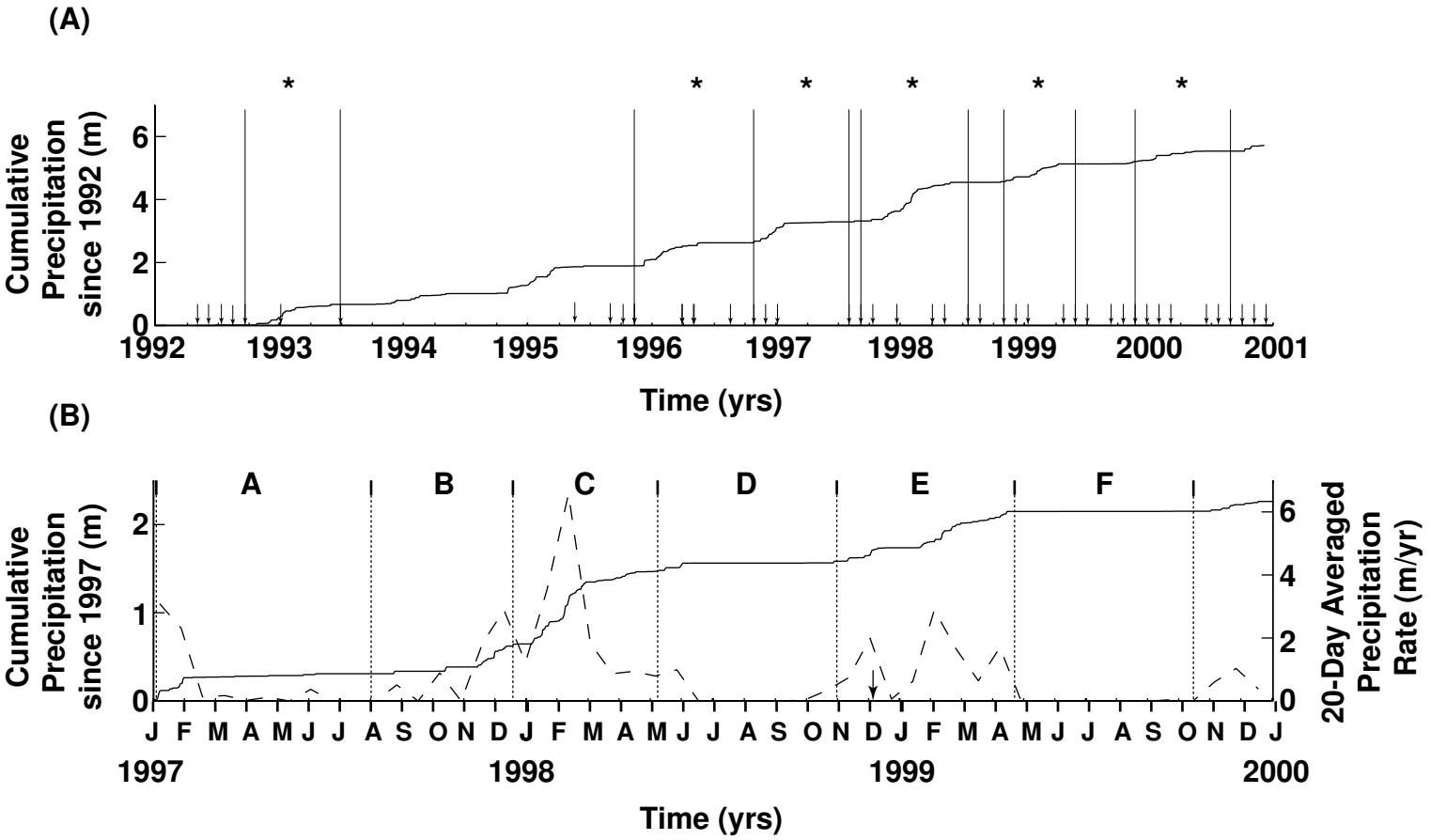
(A)
Cumulative Precipitation since 1992 (m)
0
2
4
6
1992
1993
1994
1995
1996
1997
1998
1999
2000
2001
Time (yrs)
(B)
A
B
C
D
E
F
Cumulative Precipitation since 1997 (m)
0
1
2
20-Day Averaged Precipitation Rate (m/yr)
0
2
4
6
J F M A M J J A S O N D J F M A M J J A S O N D J F M A M J J A S O N D J
1997
1998
1999
2000
Time (yrs)

Sfigure 1

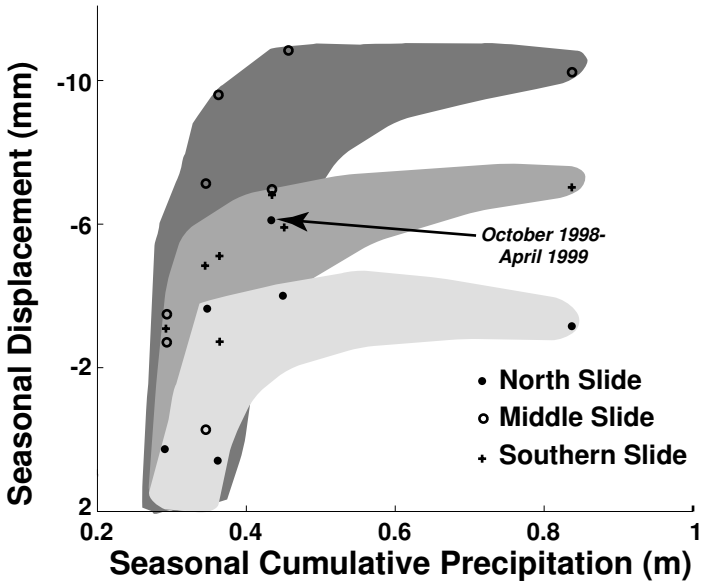
Seasonal Displacement (mm)
-10
-6
-2
2
0.2
0.4
0.6
0.8
1
Seasonal Cumulative Precipitation (m)
October 1998-
April 1999
North Slide
Middle Slide
Southern Slide

Sfigure 2

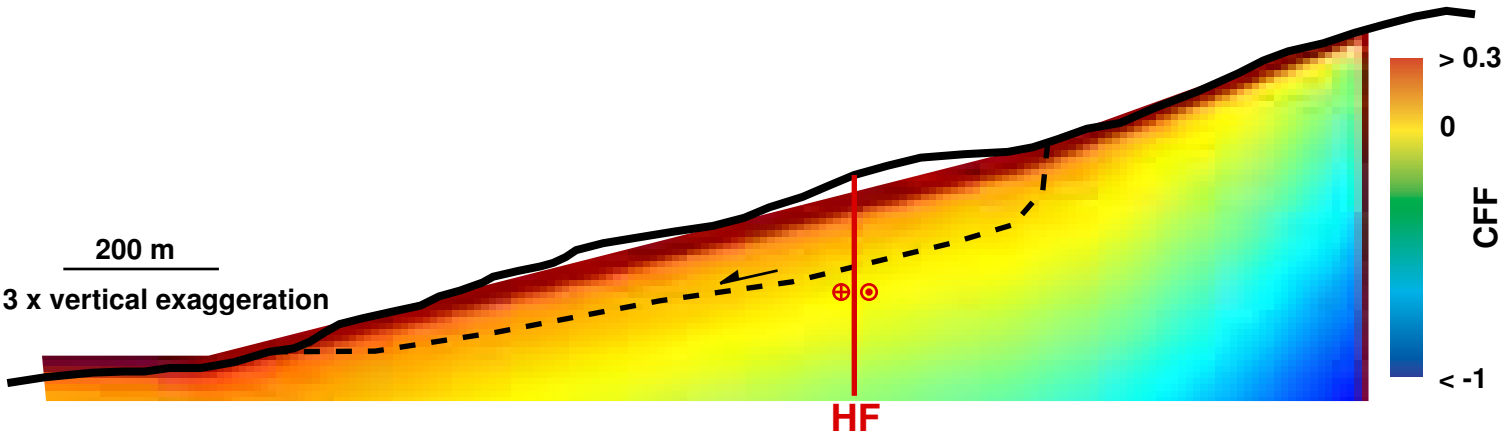

Sfigure 3